ACS APPLIED ELECTRONIC MATERIALS

pubs.acs.org/acsaelm Article

Modulation of the Metal−Nonmetal Crossover in $SrIrO_3/CaMnO_3$ Superlattices

Minghui Gu, Ruixue Zhu, Xinxin Zhang, Zhenzhen Wang, Qichang An, Fang Yang, Xiaoran Liu, Peng Gao, Meng Meng,* and Jiandong Guo*

Cite This: *ACS Appl. Electron. Mater.* 2022, 4, 3707−3713 Read Online

ACCESS | Metrics & More | Article Recommendations | Supporting Information

ABSTRACT: Due to a combination of the interplay between electron−electron correlation (EEC) and spin−orbit coupling, 3d−5d transition-metal oxide interfaces have been an intriguing platform for the exploration of emergent quantum phenomena. In this work, we investigate the 3d−5d electron coupling by designing $SrIrO_3/CaMnO_3$ superlattices and studying their electrical transport behaviors. The $[(SrIrO_3)_n/(CaMnO_3)_n]_m$ superlattices show a metal−nonmetal crossover (MNC) with the critical temperature increasing monotonically with decreasing n, until n = 1, a nonmetallic behavior is observed up to room temperature. Detailed analyses reveal that the MNC is the consequence of the weak localization modified by the enhanced EEC in $SrIrO_3$ competing with the effective field of spin−orbital relaxation, with the interfaces with $CaMnO_3$ being introduced to the superlattices. This study provides a framework for understanding the microscopic picture of 3d−5d electron coupling.

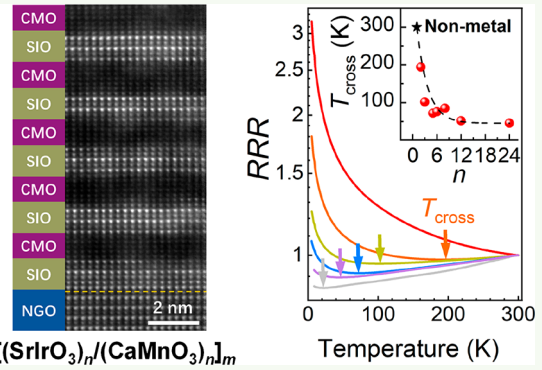

KEYWORDS: *transition-metal oxide interface, superlattices, electron−electron interaction, spin−orbital coupling, weak localization*

INTRODUCTION

Reconstructions of charge, spin, and orbital states at transition-metal oxide interfaces give rise to exotic electronic states that are absent in their bulk counterparts.[1−5] Recently, 3d−5d heterostructures have attracted considerable attention due to the coupling between spin−orbit coupling (SOC) and electron−electron correlation (EEC), in which a variety of intriguing phenomena have been realized, including a Slater insulator phase,[6,7] perpendicular magnetic anisotropy,[8−10] topological Hall effect,[11−14] and spin−orbit torque.[15,16] For instance, by variation of the epitaxial strain, a Slater−Mott crossover has been observed in superlattices of $(SrIrO_3)_1/(SrTiO_3)_1$,[7] tuning of chiral magnetic interactions by a change in the interfacial terminations has been realized in $LaMnO_3/SrIrO_3$ (SIO) heterostructures,[11] and a ferromagnetic state with $T_c \approx 100$ K could be induced in SIO via charge transfer at the $LaCoO_3$/SIO interface.[17]

As a prototypical 5d oxide, SIO has a relatively weak EEC (∼0.5 eV) and strong SOC (∼0.4 eV) in comparison with common 3d complex oxides.[18−22] It is semimetallic[23] and topologically robust, since the combination of SOC and lattice symmetry generates the protected Dirac nodal line.[24] Upon reduction of the SIO thickness, its transport behavior evolves from the semimetallic to a correlated insulating state with a critical thickness (t_c) of ∼4 unit cells (uc). Such a dimensionality-driven metal−insulator transition (MIT) in SIO has been attributed to a gap opening accompanied by the formation of a canted antiferromagnetic (AFM) ordering.[25] By introduction of a heterointerface with 3d systems, the dimensionality tailoring and strain engineering of SIO-based heterostructures also have been shown to be effective ways to modulate their transport and magnetic properties.[7,9,10,26,27] For instance, superlattices (SLs) of m-uc SIO separated by monolayers of insulating $SrTiO_3$ (STO) were found to be insulating with $m \leq 3$; SLs of $(SIO)_1/(STO)_1$ were demonstrated to be less insulating with increasing compressive strain, even to the extent of the appearance of metallicity when $(SIO)_1/(STO)_1$ SLs were grown on $NdGaO_3$ (NGO) substrates.[7] The SIO/manganite heterostructures remain a nonmetal with an SIO thickness of up to 12 uc,[11,22] indicating that 3d electrons at the interface could effectively affect the band structure of 5d-iridates. In $LaMnO_3$/SIO, 3d−5d coupling was manifested by the charge transfer from Ir to Mn,[28−30] while another work attributed the coupling effects to the formation of a Ir−Mn molecular orbital without charge transfer.[31] The mechanism of 3d−5d electron coupling is still unresolved. A further investigation of the nature of exotic behaviors of the SIO-based heterostructures is essential to fully understand the role of 3d−5d electron correlation at the interface.

Received: May 18, 2022
Accepted: July 3, 2022
Published: July 15, 2022

https://doi.org/10.1021/acsaelm.2c00655
ACS Appl. Electron. Mater. 2022, 4, 3707−3713

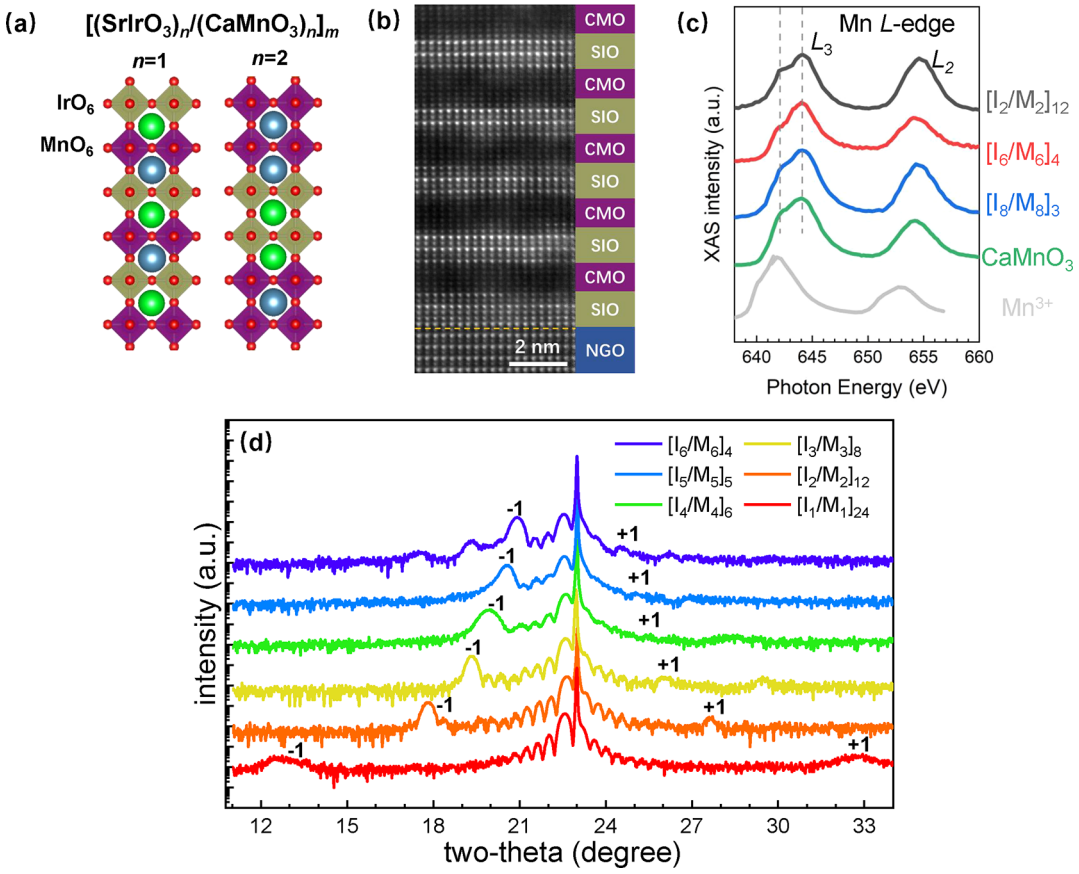

Figure 1. (a) Schematic illustration of $[I_n/M_n]_m$ SLs (n = 1, 2). IrO_6 and MnO_6 octahedra are shown in dark yellow and purple, respectively. (b) TEM image of $[I_3/M_3]_8$ SL. (c) Mn L-edge XAS of the $[I_n/M_n]_m$ SLs. The XAS of Mn^{3+} is shown for comparison.[33] (d) X-ray diffraction data of $[I_n/M_n]_m$ SLs. The first-order satellite peaks from each curve are labeled +1 and −1, respectively.

In this article, we systematically investigate the electrical transport properties of high-quality $[(SrIrO_3)_n/(CaMnO_3)_n]_m$ SLs (referred to as $[I_n/M_n]_m$). X-ray absorption spectroscopy (XAS) results indicate that there is no charge transfer between Ir and Mn ions across the interface. $[I_1/M_1]_{24}$ shows nonmetallic behavior, while SLs with $n \geq 2$ exhibit metallic characteristics at high temperatures with the metal−nonmetal crossover (MNC) temperature (referred as T_{cross}) decreasing monotonically with increasing n. The coupling between $CaMnO_3$ (CMO) 3d electrons and SIO 5d electrons illustrates Fermi liquid behavior, which is an indicator of EEC. In addition, detailed analyses of the electrical transport data indicate that the 3d electrons of CMO can also increase weak localization of SIO 5d electrons through tuning the effective fields of spin−orbital relaxation length. Our findings provide an effective regulation method to tune electron interactions in 3d−5d heterostructures.

EXPERIMENTAL METHODS

A series of $[(SrIrO_3)_n/(CaMnO_3)_n]_m$ SLs (referred to as $[I_n/M_n]_m$, where I denotes $SrIrO_3$ and M denotes $CaMnO_3$) were grown by pulsed laser deposition (PLD) on $NdGaO_3$ (110) (referred as NGO (110)) substrates (KrF excimer laser, λ = 248 nm). The growth was monitored by *in situ* reflective high-energy electron diffraction (RHEED), and the thickness was determined by counting the number of RHEED oscillations. The laser fluence and repetition rate were set as 1.5 J/cm^2 and 2 Hz, respectively. The oxygen partial pressure was optimized at 10 Pa, and the growth temperature was 670 °C. To avoid possible degradation of the samples in the atmosphere, amorphous STO capping layers were deposited at room temperature after growth. X-ray diffraction (XRD) was carried out using a Rigaku SmartLab (9 kW) X-ray diffractometer with a Ge (220) ×2 crystal monochromator. The Mn L-edge XAS measurements in total fluorescence mode were performed at beamline BL08U1A of the Shanghai Synchrotron Radiation Facility. For scanning transmission electron microscopy (STEM) image acquisition, the cross-sectional STEM specimens were thinned to less than ∼30 μm first by using mechanical polishing and then by performing argon ion milling. The ion-beam milling was carried out using a PIPS instrument (Model 691, Gatan Inc.) with an accelerating voltage of 3.5 kV until a hole was made. Low-voltage milling was performed with an accelerating voltage of 0.3 kV to remove the surface amorphous layer and to minimize damage. High-resolution high-angle annular dark-field (HAADF) images were recorded at 300 kV using an aberration-corrected FEI Titan Themis G2 instrument with a convergence semiangle for imaging of 30 mrad and collection semiangles of 39 to 200 mrad. The electrical transport properties were revealed by the a Quantum Design Physical Property Measurement System (PPMS) using a Van der Pauw geometry.

RESULTS AND DISCUSSION

Paramagnetic and semimetallic SIO has an orthorhombic structure with the pseudocubic lattice parameter a_{pc} = 3.96 Å (pc denotes pseudocubic).[32] $CaMnO_3$ (CMO) is an antiferromagnetic insulator with space group *Pbnm* and the pseudocubic lattice parameter a_{pc} = 3.73 Å.[20] NGO (110) was chosen as the substrate for growing $[I_n/M_n]_m$ SLs because its lattice constant (a_{pc} = 3.858 Å) is between SIO and CMO. In the current work, $[I_n/M_n]_m$ SLs with n = 1−24 and the layer repetition m were designed to create a total thickness of m ×

https://doi.org/10.1021/acsaelm.2c00655
ACS Appl. Electron. Mater. 2022, 4, 3707−3713

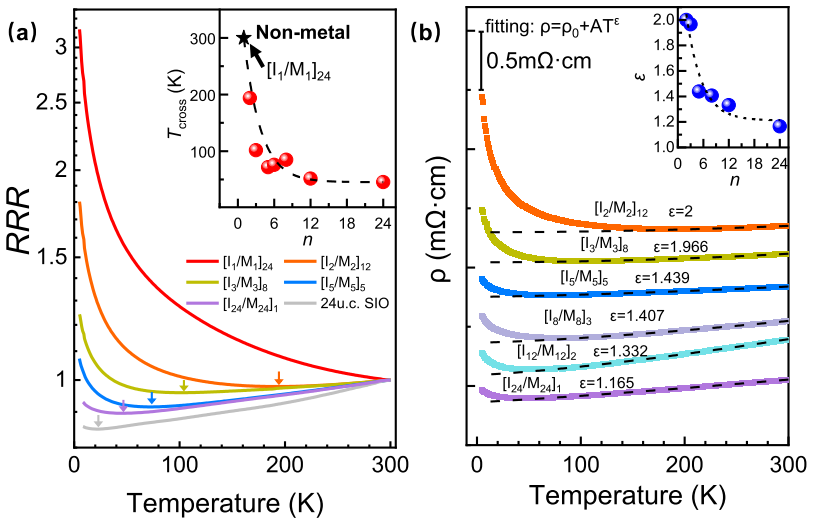

Figure 2. (a) Temperature-dependent ratio of $R(T)$ and $R(300\ K)$ (RRR) of the $[I_n/M_n]_m$ SLs. The T_{cross} value of each sample is marked by arrows. The inset shows the T_{cross} value as a function of n. The $[I_1/M_1]_{24}$ sample represents nonmetallic behavior at room temperature (indicated by a black arrow). The black dashed line is a guide for the eye. (b) Temperature-dependent resistivity of $[I_n/M_n]_m$ SLs. The black dashed curves show fitting results using $\rho = \rho_0 + AT^\varepsilon$ for each SL (curves have been offset for easier viewing). The inset shows the relationship between ε and n. The black dashed line is a guide for the eye.

$2n$ = 48 uc (24-uc SIO and 24-uc CMO, Figure 1a). Figure 1b displays the HAADF-STEM image of $[I_3/M_3]_8$ along the $[110]_{pc}$ direction. The layer-by-layer growth (see SI-I in the Supporting Information) leads to an atomically sharp interface between the NGO substrate and SIO with negligible intermixing between CMO and SIO. Figure 1d displays the high-resolution XRD $2\theta-\omega$ pattern of the SLs. Zeroth-order superlattice peaks, which is close to the NGO (110) substrate peak, are observed for all SLs. In addition, the Kiessig fringes and clear first-order satellite peaks indicate the sharp interfaces and the high crystalline quality of the SLs. The *in situ* RHEED patterns and X-ray reflectivity (XRR) results also show the high quality of $[I_n/M_n]_m$ samples (SI-Ib,c). Also, the reciprocal space mapping (RSM) of $[I_1/M_1]_{24}$ SL (SI-Id) indicates that it is coherently strained to the NGO substrate. Since all of the SLs have similar thicknesses (~48 uc) and the only variation is the change of period, the RSM result indicates that all SLs are in the same strain state.

We further investigated the possible charge transfer across the SIO/CMO interface by XAS. Figure 1c shows the Mn L-edge XAS results. In comparison with the 24-uc CMO film, there is no noticeable peak shifts or shape variation of either the Mn L_3-edge peak (~644 eV with a prepeak at ~642 eV) or the L_2-edge peak (~654 eV) in $[I_n/M_n]_m$ superlattices. Moreover, there is no peak shift with a variation of n. This indicates that the valence of Mn ions in $[I_n/M_n]_m$ superlattices is no different from that in bulk CMO, i.e., there is no charge transfer between Mn^{4+} and Ir^{4+}, consistent with a previous report by Zhang et al.[31] In addition, the peak position of Mn^{3+} ions (gray line, from ref 33) is totally different with those from SLs and the CMO reference sample (Mn^{4+}), further indicating that there is no charge transfer between SIO and CMO.

Figure 2a displays the temperature-dependent ratio of $R(T)$ and $R(300\ K)$ (RRR) of the $[I_n/M_n]_m$ samples. We also plotted the RRR value of a 24-uc SIO film in Figure 2a as a reference. It is found that there is a clear resistance minimum (defined as the MNC temperature, T_{cross}) for the SIO film at ~21.3 K, while T_{cross} increases to ~45.4 K on interfacing with the CMO layer ($[I_{24}/M_{24}]_1$, n = 24). The T_{cross} values of $[I_n/M_n]_m$ samples increase with decreasing n. For example, the T_{cross} value of $[I_{12}/M_{12}]_2$ is ~52 K and the curve of $[I_5/M_5]_5$ shows a similar trend with $T_{cross} \approx 71$ K. When n = 2, the sample exhibits a metallic character at high temperatures and has a clear resistance minimum at around 193 K. Until n = 1, the RRR value of $[I_1/M_1]_{24}$ monotonically increases with decreasing temperature, manifesting a nonmetal behavior below 300 K. We summarize the T_{cross} value as a function of n in the inset of Figure 2a, which shows that, except for the nonmetallic $[I_1/M_1]_{24}$, the SLs exhibit an n-dependent MNC behavior with $n \geq 2$.

Perovskite SIO is a narrow-band semimetal,[23] while thin SIO films may show nonmetallic characteristics at low temperatures. Reference 25 reports that a SIO film thinner than 4 uc is an insulator because of the opening of a Mott gap, while a 6-uc SIO film shows MNC behavior with $T_{cross} \approx 30$ K because of the dimensionality-driven weak localization. However, for the SLs studied in the current work, the MNC behaviors are distinctly different. First, the R_s values of all the SLs are lower than 25 kΩ (h/e^2; see SI-II), indicating that the gap-opening mechanism[25,34] could be ruled out according to the Ioffe–Regel rule.[25,34] Moreover, the T_{cross} value is higher than that of a single SIO film with the same thickness when $n \geq 6$, which indicates the different mechanisms of weak localization (SI-III and SI-IV, neither a variable range hopping model nor a dimensional crossover). On consideration of the distinct structure of the SLs with the 3d–5d interfaces, the enhanced EEC brought about by 3d electrons must prominently modulate the weak localization behavior of the SLs.

To analyze the EEC characteristics in the SLs, we fit the electrical resistivity as a function of temperature in the metallic region with the Fermi liquid model, which can be expressed as $\rho = \rho_0 + AT^\varepsilon$, where ρ_0 represents the residual resistivity brought by defects due to electron-impurity scattering at 0 K, A is the temperature coefficient of resistivity representing the inelastic scattering strength between electrons, and ε is a real number representing the intensity of EEC. When the value of ε approaches 2, it describes a system that exhibits typical Fermi

https://doi.org/10.1021/acsaelm.2c00655
ACS Appl. Electron. Mater. 2022, 4, 3707–3713

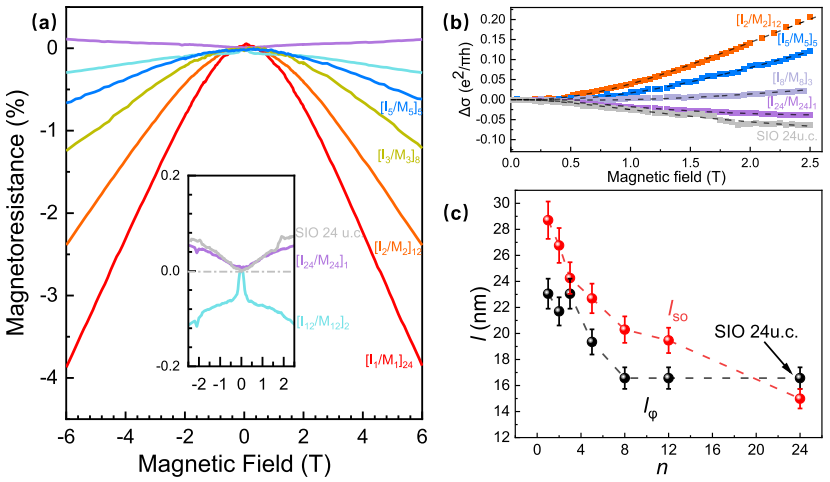

Figure 3. (a) Magnetoresistance (MR) in a perpendicular magnetic field of $[I_n/M_n]_m$ SLs and a 24-uc SIO film (measured at 5 K). The inset is the enlarged MR of $[I_{12}/M_{12}]_2$ and $[I_{24}/M_{24}]_1$ SLs and the 24-uc SIO film. (b) Magnetoconductance ($\Delta\sigma$) of representative $[I_n/M_n]_m$ SLs and the 24-uc SIO film in units of $e^2/\pi h$ as a function of magnetic field at 5 K. The best fitting results using the Maekawa−Fukuyama formula are illustrated by black dashed lines. (c) The extracted inelastic scattering lengths (l_φ) and spin−orbit relaxation lengths (l_{so}) of each sample as a function of n.

liquid behaviors with a pronounced EEC.[35−40] Figure 2b shows the resistivity as a function of temperature and the corresponding fitting curves (black dashed lines) of the $[I_n/M_n]_m$ samples. It reveals that, when $n = 24$, the fitted $\varepsilon = 1.165$, which is close to the value of a 30-uc SIO film[41] ($\varepsilon = 0.9$), indicates that $[I_{24}/M_{24}]_1$ is away from the Fermi liquid system. ε gradually increases with decreasing n (inset of Figure 2b), indicating that the EEC in the SIO blocks gets stronger when the number of SIO/CMO interfaces is increased. When $n = 2$, $[I_2/M_2]_{12}$ can be well fitted with $\varepsilon = 2$, together with an A value on the order of 10^{-9} Ω cm K^{-2}, indicating that it behaves like a typical strong EEC system.[35−40] These results indicate that the EEC in SIO is enhanced through introduction of the interface with 3d-CMO, which drives the $[I_n/M_n]_m$ systems to be nonmetals.

It is worth noting that, intuitively, the EEC enhancement at the 3d−5d interface should be limited to the quasi-2D form. However, there is a 3D feature in SLs, as evidenced by the continuous change of T_{cross} as a function of n. On the basis of the fact that the intrinsic characteristics of the SIO thin film shows that the T_{cross} value is lower than 30 K with a thickness of above 6 uc, if the EEC enhancement were quasi-2D, the T_{cross} of SLs would exhibit an abrupt change when n is above a certain value and then roughly saturate (below 30 K) as n increases.

MR analyses were carried out to reveal the weak localization mechanism. Figure 3a displays the MR of SLs in a perpendicular magnetic field between ±6 T at 5 K. As the reference, the MR of a 24-uc SIO is shown in the inset of Figure 3a. Both the 24-uc SIO film and the $[I_{24}/M_{24}]_1$ SL show positive MR, indicating the existence of weak antilocalization.[25] The SLs exhibit negative MR with $n \leq 12$, which manifests the weak localization.[34,42] Note that the weak localization ($n = 12$) to weak antilocalization ($n = 24$) crossover in SIO/CMO SLs is totally different from that in single SIO films (between 5-uc and 6-uc due to a dimensional crossover[25]). The MR percentage is the largest (∼−4% at ±6 T) for $[I_1/M_1]_{24}$, and it steadily decreases with increasing n. At $n = 12$, MR = −0.3% (at ±6 T). The MR percentages of $[I_5/M_5]_5$, $[I_8/M_8]_3$, and $[I_{12}/M_{12}]_2$ are below 1%, which are close to the values of typical weak localization systems,[34] as shown in the inset of Figure 3a. On consideration that the EEC is strengthened (represented by the increasing ε value as shown in the inset of Figure 2b) with decreasing n, the above MR analyses evidence the correlation of the enhanced EEC and the weak localization in the SLs.

To explore the mechanism of the weak localization modulation, we fit the magnetoconductance ($\Delta\sigma$) data with the Maekawa−Fukuyama formula, which can be applied to the diffusive regime that describes the change of conductivity in magnetic field with negligible Zeeman splitting[25,28,43]

$$\frac{\Delta\sigma(B)}{\sigma_0} = -\psi\left(\frac{1}{2} + \frac{B_e}{B}\right) + \frac{3}{2}\psi\left(\frac{1}{2} + \frac{B_\varphi + B_{so}}{B}\right) - \frac{1}{2}\psi\left(\frac{1}{2} + \frac{B_\varphi}{B}\right) - \ln\left(\frac{B_\varphi + B_{so}}{B_e}\right) - \frac{1}{2}\ln\left(\frac{B_\varphi + B_{so}}{B_\varphi}\right) \quad (1)$$

where ψ is the digamma function, $\sigma_0 = e^2/\pi h$ is the quantum of conductance, and B_e, B_φ, and B_{so} are the effective fields of the elastic scattering, inelastic scattering, and spin−orbit relaxation, respectively. Note that, for convenience, the effective field B_i is often expressed in terms of scattering length l_i with the relation of $B_i = \hbar/4el_i^2$. The fitting results are shown in Figure 3b (black dashed lines), and Figure 3c. There is an inversion of $l_\varphi < l_{so}$ ($n = 12$) and $l_\varphi > l_{so}$ ($n = 24$), corresponding to the crossover of weak localization and weak antilocalization,[25] which is also demonstrated by the sign change of MR (from negative with $n = 12$ to positive with $n = 24$). The l_φ value remains roughly unchanged with varying n, with only a slight increase when $n \leq 5$, which could be ascribed to the interlayer coupling.[38] With a decrease in n, the l_{so} value increases, i.e., the effective field of SOC (B_{so}) decreases, manifesting the anticorrelation of EEC and SOC, i.e., an enhanced EEC can suppress SOC and vice versa. Therefore, the modulation of the MNC in the SLs can be ascribed to the competition between EEC and SOC that determines the characteristics of the weak localization. In addition, since the SOC is intrinsically 3D, the interaction

https://doi.org/10.1021/acsaelm.2c00655
ACS Appl. Electron. Mater. 2022, 4, 3707−3713

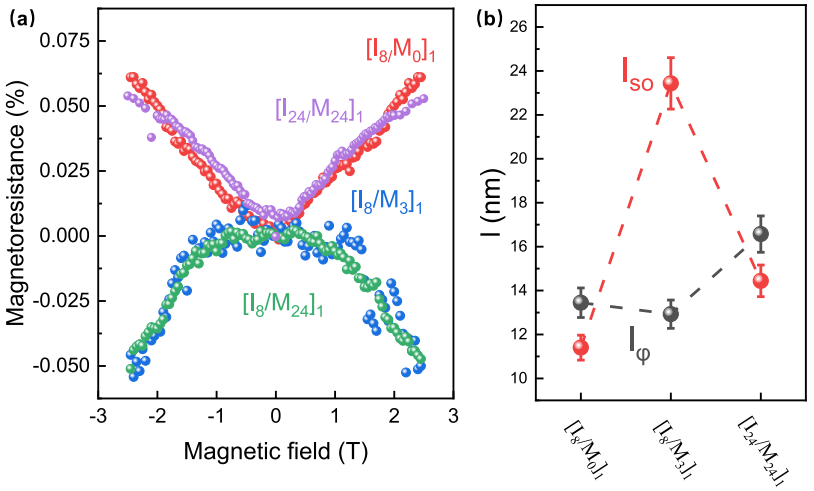

Figure 4. (a) Magnetoresistance (MR) in a perpendicular magnetic field of $[I_8/M_0]_1$, $[I_8/M_3]_1$, $[I_8/M_{24}]_1$, and $[I_{24}/M_{24}]_1$ bilayers (measured at 5 K). (b) The extracted inelastic scattering lengths (l_φ) and spin−orbit relaxation lengths (l_{so}) of $[I_8/M_0]_1$ and $[I_8/M_3]_1$. The data for $[I_{24}/M_{24}]_1$ is shown as a reference.

between SOC and EEC results in the EEC enhancement beyond the 2D limit in SIO.

We further determine the length scale of SOC affecting the EEC enhancement quantitatively by comparing the MR of several reference samples of SIO/CMO bilayers. Figure 4a illustrates the MR of $[I_8/M_0]_1$, $[I_8/M_3]_1$, $[I_8/M_{24}]_1$, and $[I_{24}/M_{24}]_1$ as a function of the magnetic field at 5 K. The MR of $[I_8/M_0]_1$ is positive, while both $[I_8/M_3]_1$ or $[I_8/M_{24}]_1$ show a negative MR, as observed in our SL samples. It is indicated that 3d electrons from CMO could effectively increase the effective fields of the spin−orbital relaxation length of at least 8-uc SIO. However, the MR would change the sign again from negative ($[I_8/M_{24}]_1$) to positive ($[I_{24}/M_{24}]_1$) when the SIO thickness is increased, illustrating that 3d electrons from CMO could not fully influence the 24-uc SIO. We also fitted the magnetoconductance data of these reference samples using eq 1, as shown in Figure 4b. The relative strengths of l_φ and l_{so} are consistent with the change of sign of MR and directly indicate that the critical thickness of 5d electrons influenced by 3d electrons is between 8-uc and 24-uc.

CONCLUSIONS

In conclusion, the high-quality epitaxial $[I_n/M_n]_m$ SLs exhibit MNC behaviors with a variation of critical temperature T_{cross} with n. Detailed investigations of the electric transport and MR indicate that the nonmetallic property of SIO can be ascribed to the weak localization significantly modulated by the interfaces with CMO. With a decrease in n, the EEC enhancement in SIO becomes more prominent, while the SOC of SIO is weakened. It is then clarified that the competition between EEC and SOC determines the weak localization of the SLs, resulting in the tunable MNC. The proposed microscopic picture of the 3d−5d electron coupling may inspire in-depth investigations of the tuning of metal−insulator transitions in complex oxides.

ASSOCIATED CONTENT

Supporting Information

The Supporting Information is available free of charge at https://pubs.acs.org/doi/10.1021/acsaelm.2c00655.

RHEED oscillations, RHEED patterns of SLs, RSM and XRR spectra of SLs, R_s-T curves of SLs and CMO, $M-H$ and $M-T$ curves of SLs and NGO substrates, VRH model fitting results of SLs, and 2D weak localization fitting results of SLs (PDF)

AUTHOR INFORMATION

Corresponding Authors

Meng Meng − *Beijing National Laboratory for Condensed Matter Physics and Institute of Physics, Chinese Academy of Sciences, Beijing 100190, People's Republic of China; Songshan Lake Materials Laboratory, Dongguan, Guangdong 523000, People's Republic of China;* orcid.org/0000-0003-3056-8257; Email: mengm@iphy.ac.cn

Jiandong Guo − *Beijing National Laboratory for Condensed Matter Physics and Institute of Physics, Chinese Academy of Sciences, Beijing 100190, People's Republic of China; School of Physical Sciences, University of Chinese Academy of Sciences, Beijing 100049, People's Republic of China; Songshan Lake Materials Laboratory, Dongguan, Guangdong 523000, People's Republic of China;* orcid.org/0000-0002-7893-022X; Email: jdguo@iphy.ac.cn

Authors

Minghui Gu − *Beijing National Laboratory for Condensed Matter Physics and Institute of Physics, Chinese Academy of Sciences, Beijing 100190, People's Republic of China; School of Physical Sciences, University of Chinese Academy of Sciences, Beijing 100049, People's Republic of China*

Ruixue Zhu − *International Center for Quantum Materials, and Electron Microscopy Laboratory, School of Physics, Peking University, Beijing 100871, People's Republic of China*

Xinxin Zhang − *International Center for Quantum Materials, and Electron Microscopy Laboratory, School of Physics, Peking University, Beijing 100871, People's Republic of China*

Zhenzhen Wang − *Beijing National Laboratory for Condensed Matter Physics and Institute of Physics, Chinese Academy of Sciences, Beijing 100190, People's Republic of China; School of Physical Sciences, University of Chinese*

https://doi.org/10.1021/acsaelm.2c00655
ACS Appl. Electron. Mater. 2022, 4, 3707−3713

Academy of Sciences, Beijing 100049, People's Republic of China

Qichang An − *Beijing National Laboratory for Condensed Matter Physics and Institute of Physics, Chinese Academy of Sciences, Beijing 100190, People's Republic of China; School of Physical Sciences, University of Chinese Academy of Sciences, Beijing 100049, People's Republic of China*

Fang Yang − *Beijing National Laboratory for Condensed Matter Physics and Institute of Physics, Chinese Academy of Sciences, Beijing 100190, People's Republic of China;* orcid.org/0000-0003-4855-585X

Xiaoran Liu − *Beijing National Laboratory for Condensed Matter Physics and Institute of Physics, Chinese Academy of Sciences, Beijing 100190, People's Republic of China*

Peng Gao − *International Center for Quantum Materials, and Electron Microscopy Laboratory, School of Physics, Peking University, Beijing 100871, People's Republic of China;* orcid.org/0000-0003-0860-5525

Complete contact information is available at: https://pubs.acs.org/10.1021/acsaelm.2c00655

Notes

The authors declare no competing financial interest.

■ ACKNOWLEDGMENTS

This work was supported by the National Key R&D Programme of China (2021YFA0718700, 2017YFA0303600), the National Natural Science Foundation of China (12104494, 11974409), and the Strategic Priority Research Program of Chinese Academy of Sciences (XDB33000000). M.M. was supported by the Youth Innovation Promotion Association, CAS. The authors acknowledge the Centre for Materials Genome, Beijing. R.Z., X.Z., and P.G. were supported by the National Natural Science Foundation of China (11974023, 52021006), the Key-Area Research and Development Program of Guangdong Province (2018B030327001, 2018B010109009), and the "2011 Program" from the Peking-Tsinghua-IOP Collaborative Innovation Center of Quantum Matter. The authors acknowledge the Electron Microscopy Laboratory of Peking University for the use of electron microscopes.

■ REFERENCES

(1) Zubko, P.; Gariglio, S.; Gabay, M.; Ghosez, P.; Triscone, J. M. Interface Physics in Complex Oxide Heterostructures. *Annu. Rev. Condens. Matter Phys.* **2011**, *2*, 141−165.

(2) Streltsov, S. V.; Khomskii, D. I. Orbital physics in transition metal compounds: new trends. *Phys. Usp.* **2017**, *60*, 1121−1146.

(3) Tokura, Y.; Nagaosa, N. Orbital physics in transition-metal oxides. *Science* **2000**, *288*, 462−468.

(4) Ramesh, R.; Schlom, D. G. Creating emergent phenomena in oxide superlattices. *Nat. Rev. Mater.* **2019**, *4*, 257−268.

(5) Hwang, H. Y.; Iwasa, Y.; Kawasaki, M.; Keimer, B.; Nagaosa, N.; Tokura, Y. Emergent phenomena at oxide interfaces. *Nat. Mater.* **2012**, *11*, 103−113.

(6) Cui, Q.; Cheng, J. G.; Fan, W.; Taylor, A. E.; Calder, S.; McGuire, M. A.; Yan, J. Q.; Meyers, D.; Li, X.; Cai, Y. Q.; Jiao, Y. Y.; Choi, Y.; Haskel, D.; Gotou, H.; Uwatoko, Y.; Chakhalian, J.; Christianson, A. D.; Yunoki, S.; Goodenough, J. B.; Zhou, J. S. Slater Insulator in Iridate Perovskites with Strong Spin-Orbit Coupling. *Phys. Rev. Lett.* **2016**, *117*, 176603.

(7) Yang, J.; Hao, L.; Meyers, D.; Dasa, T.; Xu, L.; Horak, L.; Shafer, P.; Arenholz, E.; Fabbris, G.; Choi, Y.; Haskel, D.; Karapetrova, J.; Kim, J. W.; Ryan, P. J.; Xu, H.; Batista, C. D.; Dean, M. P. M.; Liu, J. Strain-Modulated Slater-Mott Crossover of Pseudospin-Half Square-Lattice in (SrIrO3)1/(SrTiO3)1 Superlattices. *Phys. Rev. Lett.* **2020**, *124*, 177601.

(8) Zeng, Z. T.; Feng, J. T.; Zheng, X.; Wang, C. H.; Liu, J. W.; Lu, Z. X.; Jiang, F. X.; Xu, X. H.; Wang, Z. M.; Li, R. W. Emergent ferromagnetism with tunable perpendicular magnetic anisotropy in short-periodic $SrIrO_3/SrRuO_3$ superlattices. *Appl. Phys. Lett.* **2020**, *116*, 142401.

(9) Yi, D.; Liu, J.; Hsu, S. L.; Zhang, L.; Choi, Y.; Kim, J. W.; Chen, Z.; Clarkson, J. D.; Serrao, C. R.; Arenholz, E.; Ryan, P. J.; Xu, H.; Birgeneau, R. J.; Ramesh, R. Atomic-scale control of magnetic anisotropy via novel spin-orbit coupling effect in $La_{2/3}Sr_{1/3}MnO_3/SrIrO_3$ superlattices. *Proc. Natl. Acad. Sci. U. S. A.* **2016**, *113*, 6397−6402.

(10) Yi, D.; Flint, C. L.; Balakrishnan, P. P.; Mahalingam, K.; Urwin, B.; Vailionis, A.; N'Diaye, A. T.; Shafer, P.; Arenholz, E.; Choi, Y.; Stone, K. H.; Chu, J. H.; Howe, B. M.; Liu, J.; Fisher, I. R.; Suzuki, Y. Tuning Perpendicular Magnetic Anisotropy by Oxygen Octahedral Rotations in $(La_{1-x}Sr_xMnO_3)/(SrIrO_3)$ Superlattices. *Phys. Rev. Lett.* **2017**, *119*, 077201.

(11) Skoropata, E.; Nichols, J.; Ok, J. M.; Chopdekar, R. V.; Choi, E. S.; Rastogi, A.; Sohn, C.; Gao, X.; Yoon, S.; Farmer, T.; Desautels, R. D.; Choi, Y.; Haskel, D.; Freeland, J. W.; Okamoto, S.; Brahlek, M.; Lee, H. N. Interfacial tuning of chiral magnetic interactions for large topological Hall effects in $LaMnO_3/SrIrO_3$ heterostructures. *Sci. Adv.* **2020**, *6*, eaaz3902.

(12) Ohuchi, Y.; Matsuno, J.; Ogawa, N.; Kozuka, Y.; Uchida, M.; Tokura, Y.; Kawasaki, M. Electric-field control of anomalous and topological Hall effects in oxide bilayer thin films. *Nat. Commun.* **2018**, *9*, 213.

(13) Meng, K. Y.; Ahmed, A. S.; Bacani, M.; Mandru, A. O.; Zhao, X.; Bagues, N.; Esser, B. D.; Flores, J.; McComb, D. W.; Hug, H. J.; Yang, F. Observation of Nanoscale Skyrmions in $SrIrO_3/SrRuO_3$ Bilayers. *Nano Lett.* **2019**, *19*, 3169−3175.

(14) Matsuno, J.; Ogawa, N.; Yasuda, K.; Kagawa, F.; Koshibae, W.; Nagaosa, N.; Tokura, Y.; Kawasaki, M. Interface-driven topological Hall effect in $SrRuO_3$-$SrIrO_3$ bilayer. *Sci. Adv.* **2016**, *2*, e1600304.

(15) Nan, T.; Anderson, T. J.; Gibbons, J.; Hwang, K.; Campbell, N.; Zhou, H.; Dong, Y. Q.; Kim, G. Y.; Shao, D. F.; Paudel, T. R.; Reynolds, N.; Wang, X. J.; Sun, N. X.; Tsymbal, E. Y.; Choi, S. Y.; Rzchowski, M. S.; Kim, Y. B.; Ralph, D. C.; Eom, C. B. Anisotropic spin-orbit torque generation in epitaxial $SrIrO_3$ by symmetry design. *Proc. Natl. Acad. Sci. U. S. A.* **2019**, *116*, 16186−16191.

(16) Liu, L.; Qin, Q.; Lin, W.; Li, C.; Xie, Q.; He, S.; Shu, X.; Zhou, C.; Lim, Z.; Yu, J.; Lu, W.; Li, M.; Yan, X.; Pennycook, S. J.; Chen, J. Current-induced magnetization switching in all-oxide heterostructures. *Nat. Nanotechnol.* **2019**, *14*, 939−944.

(17) Jaiswal, A. K.; Wang, D.; Wollersen, V.; Schneider, R.; Tacon, M. L.; Fuchs, D. Direct Observation of Strong Anomalous Hall Effect and Proximity-Induced Ferromagnetic State in $SrIrO_3$. *Adv. Mater.* **2022**, *34*, 2109163.

(18) Kim, B. J.; Jin, H.; Moon, S. J.; Kim, J. Y.; Park, B. G.; Leem, C. S.; Yu, J.; Noh, T. W.; Kim, C.; Oh, S. J.; Park, J. H.; Durairaj, V.; Cao, G.; Rotenberg, E. Novel J_{eff}=1/2 Mott state induced by relativistic spin-orbit coupling in Sr_2IrO_4. *Phys. Rev. Lett.* **2008**, *101*, 076402.

(19) Moon, S. J.; Jin, H.; Kim, K. W.; Choi, W. S.; Lee, Y. S.; Yu, J.; Cao, G.; Sumi, A.; Funakubo, H.; Bernhard, C.; Noh, T. W. Dimensionality-controlled insulator-metal transition and correlated metallic state in 5*d* transition metal oxides $Sr_{n+1}Ir_nO_{3n+1}$ (n = 1, 2, and ∞). *Phys. Rev. Lett.* **2008**, *101*, 226402.

(20) Wang, F.; Dong, B. J.; Zhang, Y. Q.; Liu, W.; Zhang, H. R.; Bai, Y.; Li, S. K.; Yang, T.; Sun, J. R.; Wang, Z. J.; Zhang, Z. D. Single orthorhombic b axis orientation and antiferromagnetic ordering type in multiferroic CaMnO3 thin film with $La_{0.67}Ca_{0.33}MnO_3$ buffer layer. *Appl. Phys. Lett.* **2017**, *111*, 122902.

(21) Vistoli, L.; Wang, W.; Sander, A.; Zhu, Q.; Casals, B.; Cichelero, R.; Barthélémy, A.; Fusil, S.; Herranz, G.; Valencia, S.; Abrudan, R.; Weschke, E.; Nakazawa, K.; Kohno, H.; Santamaria, J.;

Wu, W.; Garcia, V.; Bibes, M. Giant topological Hall effect in correlated oxide thin films. *Nat. Phys.* **2019**, *15*, 67−72.
(22) Nichols, J.; Gao, X.; Lee, S.; Meyer, T. L.; Freeland, J. W.; Lauter, V.; Yi, D.; Liu, J.; Haskel, D.; Petrie, J. R.; Guo, E. J.; Herklotz, A.; Lee, D.; Ward, T. Z.; Eres, G.; Fitzsimmons, M. R.; Lee, H. N. Emerging magnetism and anomalous Hall effect in iridate-Manganite heterostructures. *Nat. Commun.* **2016**, *7*, 12721.
(23) Nie, Y. F.; King, P. D.; Kim, C. H.; Uchida, M.; Wei, H. I.; Faeth, B. D.; Ruf, J. P.; Ruff, J. P.; Xie, L.; Pan, X.; Fennie, C. J.; Schlom, D. G.; Shen, K. M. Interplay of spin-orbit interactions, dimensionality, and octahedral rotations in semimetallic $SrIrO_3$. *Phys. Rev. Lett.* **2015**, *114*, 016401.
(24) Chen, Y.; Lu, Y. M.; Kee, H. Y. Topological crystalline metal in orthorhombic perovskite iridates. *Nat. Commun.* **2015**, *6*, 6593.
(25) Groenendijk, D. J.; Autieri, C.; Girovsky, J.; Martinez-Velarte, M. C.; Manca, N.; Mattoni, G.; Monteiro, A.; Gauquelin, N.; Verbeeck, J.; Otte, A. F.; Gabay, M.; Picozzi, S.; Caviglia, A. D. Spin-Orbit Semimetal $SrIrO_3$ in the Two-Dimensional Limit. *Phys. Rev. Lett.* **2017**, *119*, 256403.
(26) Hao, L.; Meyers, D.; Frederick, C.; Fabbris, G.; Yang, J.; Traynor, N.; Horak, L.; Kriegner, D.; Choi, Y.; Kim, J. W.; Haskel, D.; Ryan, P. J.; Dean, M. P. M.; Liu, J. Two-Dimensional J_{eff}=1/2 Antiferromagnetic Insulator Unraveled from Interlayer Exchange Coupling in Artificial Perovskite Iridate Superlattices. *Phys. Rev. Lett.* **2017**, *119*, 027204.
(27) Matsuno, J.; Ihara, K.; Yamamura, S.; Wadati, H.; Ishii, K.; Shankar, V. V.; Kee, H. Y.; Takagi, H. Engineering a Spin-Orbital Magnetic Insulator by Tailoring Superlattices. *Phys. Rev. Lett.* **2015**, *114*, 247209.
(28) Suraj, T. S.; Omar, G. J.; Jani, H.; Juvaid, M. M.; Hooda, S.; Chaudhuri, A.; Rusydi, A.; Sethupathi, K.; Venkatesan, T.; Ariando, A.; Rao, M. S. R. Tunable and enhanced Rashba spin-orbit coupling in iridate-Manganite heterostructures. *Phys.Rev.B* **2020**, *102*, 125145.
(29) Huang, K.; Wu, L.; Wang, M. Y.; Swain, N.; Motapothula, M.; Luo, Y. Z.; Han, K.; Chen, M. F.; Ye, C.; Yang, A. J.; Xu, H.; Qi, D. C.; N'Diaye, A. T.; Panagopoulos, C.; Primetzhofer, D.; Shen, L.; Sengupta, P.; Ma, J.; Feng, Z. X.; Nan, C. W.; Wang, X. R. Tailoring magnetic order via atomically stacking 3*d*/5*d* electrons to achieve high-performance spintronic devices. *Applied Physics Reviews* **2020**, *7*, 011401.
(30) Yu, T.; Deng, B.; Zhou, L.; Chen, P.; Liu, Q.; Wang, C.; Ning, X.; Zhou, J.; Bian, Z.; Luo, Z.; Qiu, C.; Shi, X. Q.; He, H. Polarity and Spin-Orbit Coupling Induced Strong Interfacial Exchange Coupling: An Asymmetric Charge Transfer in Iridate-Manganite Heterostructure. *ACS Appl. Mater. Interfaces* **2019**, *11*, 44837−44843.
(31) Zhang, Y.; Luo, Y. Z.; Wu, L.; Suzuki, M.; Zhang, Q.; Hirata, Y.; Yamagami, K.; Takubo, K.; Ikeda, K.; Yamamoto, K.; Yasui, A.; Kawamura, N.; Lin, C.; Koshiishi, K.; Liu, X.; Zhang, J.; Hotta, Y.; Wang, X. R.; Fujimori, A.; Lin, Y.; Nan, C.; Shen, L.; Wadati, H. Interfacial-hybridization-modified Ir ferromagnetism and electronic structure in $LaMnO_3/SrIrO_3$ superlattices. *Phys. Rev. Res.* **2020**, *2*, 033496.
(32) Longo, J. M.; Kafalas, J. A.; Arnott, R. J. Structure and properties of the high and low pressure forms of $SrIrO_3$. *J. Solid State Chem.* **1971**, *3*, 174−179.
(33) Chen, Z.; Chen, Z.; Liu, Z. Q.; Holtz, M. E.; Li, C. J.; Wang, X. R.; Lu, W. M.; Motapothula, M.; Fan, L. S.; Turcaud, J. A.; Dedon, L. R.; Frederick, C.; Xu, R. J.; Gao, R.; N'Diaye, A. T.; Arenholz, E.; Mundy, J. A.; Venkatesan, T.; Muller, D. A.; Wang, L. W.; Liu, J.; Martin, L. W. Electron Accumulation and Emergent Magnetism in $LaMnO_3/SrTiO_3$ Heterostructures. *Phys. Rev. Lett.* **2017**, *119*, 156801.
(34) Scherwitzl, R.; Gariglio, S.; Gabay, M.; Zubko, P.; Gibert, M.; Triscone, J. M. Metal-insulator transition in ultrathin $LaNiO_3$ films. *Phys. Rev. Lett.* **2011**, *106*, 246403.
(35) Hu, L.; Wei, R. H.; Yan, J.; Wang, D.; Tang, X. W.; Luo, X.; Song, W. H.; Dai, J. M.; Zhu, X. B.; Zhang, C. J.; Sun, Y. P. $La_{2/3}Sr_{1/3}VO_3$ Thin Films: A New p-Type Transparent Conducting Oxide with Very High Figure of Merit. *Adv. Electron. Mater.* **2018**, *4*, 1700476.
(36) Sheets, W. C.; Mercey, B.; Prellier, W. Effect of charge modulation in $(LaVO_3)_m(SrVO_3)_n$ superlattices on the insulator-metal transition. *Appl. Phys. Lett.* **2007**, *91*, 192102.
(37) Takayanagi, M.; Tsuchiya, T.; Namiki, W.; Ueda, S.; Minohara, M.; Horiba, K.; Kumigashira, H.; Terabe, K.; Higuchi, T. Unexpected metal-insulator transition in thick $Ca_{1-x}Sr_xVO_3$ film on $SrTiO_3$ (100) single crystal. *Appl. Phys. Lett.* **2018**, *112*, 133106.
(38) Wang, J.; Gauquelin, N.; Huijben, M.; Verbeeck, J.; Rijnders, G.; Koster, G. Metal-insulator transition of $SrVO_3$ ultrathin films embedded in $SrVO_3/SrTiO_3$ superlattices. *Appl. Phys. Lett.* **2020**, *117*, 133105.
(39) Maceachern, M. J.; Dabkowska, H.; Garrett, J. D.; Amow, G.; Gong, W. H.; Liu, G.; Greedan, J. E. Metal-Insulator Transitions in $La_{1-x}TiO_3$, 0.0 ≤ X≤ 0.33. Structure-Property Correlations. *Chem. Mater.* **1994**, *6*, 2092−2102.
(40) Dao, T. M.; Mondal, P. S.; Takamura, Y.; Arenholz, E.; Lee, J. Metal-insulator transition in low dimensional $La_{0.75}Sr_{0.25}VO_3$ thin films. *Appl. Phys. Lett.* **2011**, *99*, 112111.
(41) Groenendijk, D. J.; Manca, N.; Mattoni, G.; Kootstra, L.; Gariglio, S.; Huang, Y.; van Heumen, E.; Caviglia, A. D. Epitaxial growth and thermodynamic stability of $SrIrO_3/SrTiO_3$ heterostructures. *Appl. Phys. Lett.* **2016**, *109*, 041906.
(42) Son, J.; Moetakef, P.; LeBeau, J. M.; Ouellette, D.; Balents, L.; Allen, S. J.; Stemmer, S. Low-dimensional Mott material: Transport in ultrathin epitaxial $LaNiO_3$ films. *Appl. Phys. Lett.* **2010**, *96*, 062114.
(43) Hurand, S.; Jouan, A.; Feuillet-Palma, C.; Singh, G.; Biscaras, J.; Lesne, E.; Reyren, N.; Barthelemy, A.; Bibes, M.; Villegas, J. E.; Ulysse, C.; Lafosse, X.; Pannetier-Lecoeur, M.; Caprara, S.; Grilli, M.; Lesueur, J.; Bergeal, N. Field-effect control of superconductivity and Rashba spin-orbit coupling in top-gated $LaAlO_3/SrTiO_3$ devices. *Sci. Rep.* **2015**, *5*, 12751.

https://doi.org/10.1021/acsaelm.2c00655
ACS Appl. Electron. Mater. 2022, 4, 3707−3713